PAPER

Manganese single-atom modification of MOF-808 for catalytic nerve agent and simulant degradation

Arshia Sulaiman, [iD][a] Mohammad Khurram Javed, [iD][a] Carl Fossum,[a] Conor L. Long,[b]
Matthew B. Leonard, [iD][c] Minliang Yan,[a] Mikaela C. Boyanich,[a] Naveen Kumar,[a]
Alex Balboa,[c] Hui Wang,[c] Eric M. Johnson,[a] John J. Mahle,[c]
Christopher J. Karwacki,[c] Jenny V. Lockard,[b] Diego Troya, [iD][a]
John R. Morris [iD][a] and Amanda J. Morris [iD]*[a]

The extreme toxicity of nerve agents highlights the urgent need for catalytic materials that can operate under realistic, dry conditions. Zirconium-based MOF-808 is effective for the aqueous-phase hydrolysis of these agents, but its performance drops sharply in solid-phase environments due to poisoning by tightly bound bidentate products. Here, we introduce a manganese (Mn) single-atom modified version of MOF-808 that overcomes this limitation. Unlike the native framework, Mn@MOF-808 achieves catalytic turnover (turnover number or TON > 1) for nerve agent and simulant degradation under ambient, unbuffered, and solvent-free conditions. The Mn sites help avoid product inhibition by favoring monodentate interactions over bidentate coordination. Experimental results show sustained reactivity during degradation of sarin and its simulants, and DFT calculations support reduced desorption energies of bound products. This work marks the first example of a MOF-based catalyst demonstrating turnover in solid-phase nerve agent degradation and moves a step closer to practical chemical threat mitigation.

Introduction

Nerve agents are among the most lethal chemical warfare agents, capable of causing death within minutes by disrupting the normal nerve signaling.[1–5] Although banned under the Chemical Weapons Convention, their use has been reported in recent conflicts,[4] reinforcing the urgent need for catalytic materials that can detoxify these threats quickly and effectively under realistic conditions. Zirconium (Zr)-based metal–organic frameworks (MOFs) have gained attention as promising candidates for this purpose, thanks to their chemical stability and ability to promote hydrolysis reactions.[6–15] Typically, the detoxification mechanism involves a nucleophilic attack by hydroxide, which replaces a leaving group—such as fluoride—with a hydroxyl group, thereby reducing toxicity (Fig. 1a).[16,17] However, under dry or gas-phase conditions, catalysts like MOF-808 are limited by catalyst poisoning due to deactivation by strongly bound hydrolysis products. These products often bridge adjacent Zr sites in a bidentate fashion, blocking access to active sites and halting turnover.[18–20]

To overcome this limitation, we present a modified version of MOF-808 incorporating manganese (Mn) as single atoms. This is the first MOF-based catalyst shown to achieve catalytic turnover (turnover number or TON > 1) for nerve agent and simulant degradation under solid-phase, unbuffered, and solvent-free conditions. Inspired by prior computational predictions and literature suggesting that single-atom modifications can mitigate catalyst poisoning,[21–23] we synthesized a series of Mn-modified MOF-808 catalysts (Mn@MOF-808), labeled Mn@MOF-808-*x*, where *x* corresponds to the Mn loading per node.

The introduction of Mn is hypothesized to alter the coordination preferences of hydrolysis products, shifting them toward monodentate geometries that make desorption more favorable and preserve catalytic activity. Using X-ray Absorption Spectroscopy (XAS), *in situ* Diffuse Reflectance Infrared Fourier Transform Spectroscopy (DRIFTS), and Density Functional Theory (DFT), we investigate the structural and mechanistic features underlying this behavior. Among the catalysts tested, Mn@MOF-808-1.10 uniquely supports sustained activity under solid-phase conditions.

Recent studies have begun to investigate the potential of solid-phase reactivity in Zr-MOF systems for the degradation of nerve agents and simulants. For example, fabricating MOF–hydrogel composites that retain hydrolytic activity under low-water conditions[24] and modifying MOF powders

*[a] Department of Chemistry, Virginia Tech, Blacksburg, VA, 24061, USA.
E-mail: ajmorris@vt.edu*
[b] Department of Chemistry, Rutgers University Newark, NJ, 07102, USA
[c] U.S. Army Combat Capabilities Development Command Chemical Biological Center, Aberdeen Proving Ground, MD, 21010, USA

This journal is © The Royal Society of Chemistry 2025

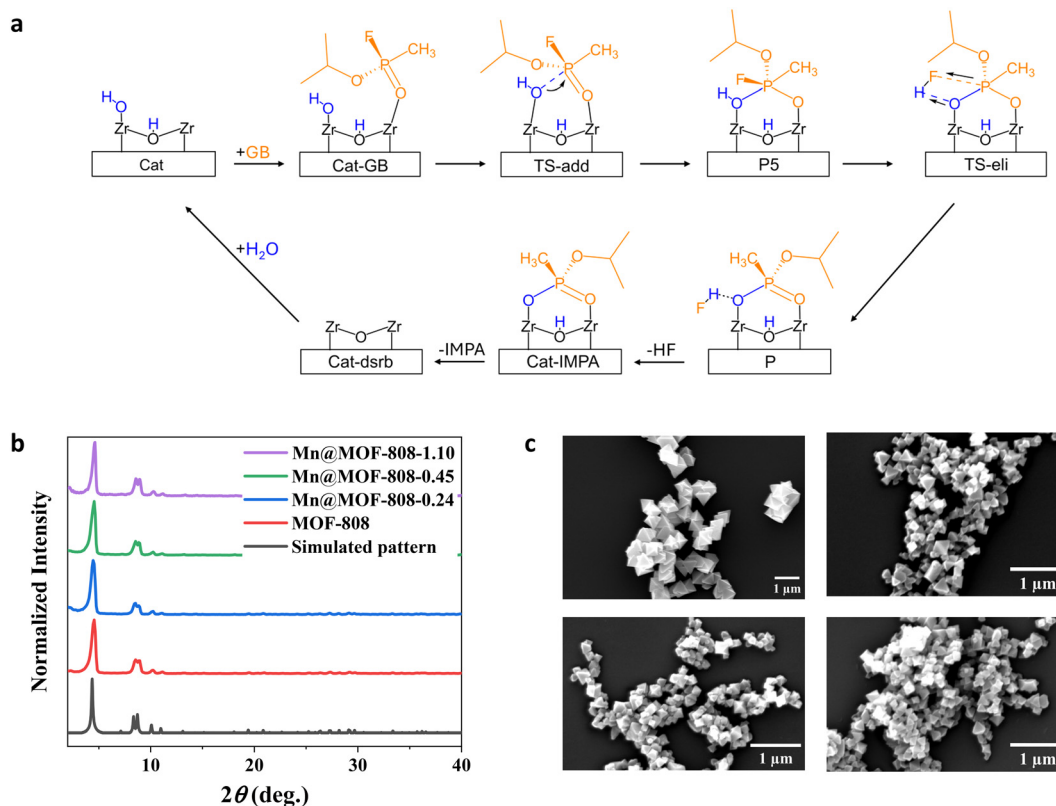*Catal. Sci. Technol.*, 2025, **15**, 7549–7557 | 7549

Fig. 1 (a) Reaction mechanism for the hydrolysis of sarin (GB) on native MOF-808. (b) PXRD patterns and (c) SEM images of i) MOF-808, ii) Mn@MOF-808-0.24, iii) Mn@MOF-808-0.45, and iv) Mn@MOF-808-1.10.

with imidazole derivatives,[25] polymeric organic amines,[26] and alcoholamine molecules[27] to enhance catalysis under high humidity conditions. While these studies highlight important progress toward practical application, they generally rely on additives (such as polymers), operate under humid or partially aqueous environments, or achieve only stoichiometric reactivity. In contrast, the work presented here demonstrates, for the first time, that single-atom modification of MOF-808 enables true catalytic turnover (TON > 1) for nerve agent and simulant degradation under completely unbuffered, solvent- and base-free solid-phase conditions.

Overall, this work demonstrates how single-atom incorporation at the MOF node can fine-tune reactivity and resist poisoning, moving MOF-based catalysts closer to practical applications in chemical defense.

Experimental

Materials and methods

All chemicals, unless otherwise stated, were purchased from commercial suppliers and used as received.

Synthesis of MOF-808. MOF-808 was prepared following previously reported methods.[28] 15.0 mmol of ZrOCl$_2$·8H$_2$O was combined with 225 mL N,N-dimethylformamide (DMF) and 225 mL formic acid in a 500 mL Pyrex jar. Subsequently, 4.9 mmol of benzene tricarboxylic acid (BTC) was added, and the solution was heated at 120 °C for 72 h. The resulting

mixture was collected via centrifugation and washed thrice with DMF. The washed sample was then suspended in DMF and soaked for 24 h. The DMF soaking process was repeated for 3 d, with fresh DMF added daily. The soaking procedure was repeated using acetone for an additional 3 d. The resulting powder was collected and dried overnight in an oven. Finally, the sample was activated by heating at 200 °C under vacuum (1 × 10^{-4} Torr).

Synthesis of Mn@MOF-808. To prepare Mn@MOF-808, 3.7 mmol of anhydrous MnCl$_2$ was combined with 12 mL DMF in a 6 dram vial. The mixture was sonicated until complete dissolution of the salt was achieved. Subsequently, 0.3 mmol of activated MOF-808 was added to the vial, and the solution was sonicated for an additional 15 min. The resulting solution was then heated at 85 °C for 3 d to yield Mn@MOF-808-0.24, at 85 °C for 7 d to produce Mn@MOF-808-0.45, and at 100 °C for 3 d to obtain Mn@MOF-808-1.10. The Mn@MOF-808 samples underwent the same post-treatment procedure as MOF-808 for activation.

Characterization methods and catalysis protocols are described in detail in the SI.

Results and discussion

Structural characterization of MOF-808 and Mn@MOF-808

MOF-808 is composed of Zr$_6$(μ_3-O)$_4$(μ_3-OH)$_4$ clusters connected to six tritopic benzene-1,3,5-tricarboxylic acid

(BTC) linkers.[28] This connectivity results in nodes with six accessible coordination sites per cluster, which can serve as potential anchoring points for single atom modification. The successful formation of the MOFs was confirmed by Powder X-ray Diffraction (PXRD). The PXRD plots (Fig. 1b) of the Mn@MOF-808 samples indicated that the bulk crystallinity remained unaffected by Mn doping. Scanning Electron Microscopy (SEM) revealed octahedral particles with sizes around 0.7–1 μm for MOF-808 and 0.1–0.4 μm for the Mn@MOF-808 samples (Fig. 1c). After single-atom modification, MOF-808 particles are smaller, likely due to partial framework disruption and recrystallization during the incorporation process. Following SEM analysis, we used High-Angle Annular Dark-Field Scanning Transition Electron Microscopy (HAADF-STEM) coupled with Energy-Dispersive X-ray Spectroscopy (EDS) to examine the distribution of Mn within the MOF framework. Elemental mapping from STEM-EDS images (Fig. S1) confirms that Mn is successfully incorporated and uniformly distributed throughout the crystallites. Additional high-magnification HAADF-STEM and elemental mapping were performed for Mn@MOF-808-1.10 to examine the distribution of Mn within MOF-808 (Fig. S2). Although atomic resolution was not achieved due to the low Mn loading, the higher-resolution images clearly show a homogeneous distribution of Mn and Zr across MOF crystallites, with no evidence of Mn clustering or phase segregation. The uniform dispersion is consistent with previous reports of single-atom incorporation in Zr-based MOFs,[29] supporting that Mn is incorporated at the Zr_6 node sites rather than forming separate Mn species. To determine the surface area, nitrogen adsorption isotherms (Fig. S3) were measured, and the Brunauer–Emmett–Teller (BET) surface area was calculated (Table S1). All MOF samples exhibited high surface areas ranging from 1300 to 2000 m^2 g^{-1}. The incremental pore volume vs. pore width plots, shown in Fig. S4, further confirm the porous nature and pore size distribution of the MOF-808 and Mn@MOF-808 samples. The thermal stability of the MOF samples is detailed in SI section S4.1 and Fig. S16. Mn loading was determined using Inductively Coupled Plasma-Mass Spectroscopy (ICP-MS), and the results are presented in Table S2. The Mn per MOF node ratios of the three modified samples, namely, Mn@MOF-808-0.24, Mn@MOF-808-0.45, and Mn@MOF-808-1.10, were determined to be 0.24 Mn/node, 0.45 Mn/node, and 1.10 Mn/node, respectively. The Mn/ratios from X-ray Photoelectron Spectroscopy (XPS) are shown in Fig. S5 and Table S3. The MOF samples were digested and analyzed via Nuclear Magnetic Resonance (NMR) to quantify the amount of formate capping the MOF nodes, in order to assess node occupancy and the extent of available open coordination sites. MOF-808 shows approximately four formates per node, suggesting the presence of two open active sites. In contrast, the Mn@MOF-808-1.10 sample has approximately five formates per node, indicating that all Zr sites are capped and the only remaining open active site is the Mn single atom. The slight increase in the formate content per node after Mn incorporation is likely

due to DMF decomposition under heating, which generates additional formates that coordinate with the Zr nodes. Details are provided in SI section S4.2, Table S9 and Fig. S17. Fourier Transform Infrared (FTIR) spectroscopy was conducted to gain insight into how the overall bonding structure of the MOF-808 may be affected by the inclusion of Mn. The similarity between the IR spectra of MOF-808 and Mn@MOF-808-1.10 indicates that the incorporation of Mn single atoms into the MOF-808 framework does not alter its structural integrity (Fig. S6).

Oxidation state and the coordination environment of Mn single atoms

The Mn K-edge XAS spectra of the Mn@MOF-808 frameworks are depicted along with relevant Mn standards in Fig. 2a. Comparison of the MOF X-ray Absorption Near-Edge Structure (XANES) spectra with those of the $MnCl_2$ and MnO references reveals a similar edge shift, suggesting an analogous oxidation state of Mn(II). XPS analysis to confirm the oxidation state of Mn is detailed in SI section S4.3 and Table S10. Fig. 2b contains an overlay of the R-space Extended X-ray Absorption Fine Structure (EXAFS) spectra for these MOFs and references. XANES and EXAFS analyses indicate that the Mn in Mn@MOF-808 adopts a distinct coordination environment compared to Mn foil, oxide, or chloride standards, suggesting unique speciation within the framework. While the Zr-edge XANES (Fig. S7a) spectra show no major changes in the Zr local environment upon Mn doping, EXAFS R-space analysis (Fig. S7c) reveals an enhanced second-shell feature above 3 Å, which may be attributed to Mn–Zr scattering.

Mn K-edge EXAFS fitting for the Mn@MOF-808-0.24 sample was carried out using a model (Fig. 2c) derived from the calculated structure, with results shown in Fig. 2d and f, and summarized in Table S4. The fitting model included the first shell O coordination environment surrounding the metal and the two closest neighboring Zr sites (Fig. 2e). While the model predicts additional contribution from Mn–Zr scattering paths (with scattering distances between 3–4 Å), a second shell peak is not observed with substantial amplitude for either MOF samples. The discrepancy is due to the contributions from multiple Mn–Zr scattering paths destructively interfering with each other, as can be seen in the plot of the real component of the calculated R space spectra associated with the two Mn–Zr scattering path contributions used in the fit (Fig. 2f). Consequently, the overall Mn–Zr scattering path intensity was severely attenuated, as can be seen in the fitting results. The results of this fitting procedure point towards a good agreement between the theoretical Mn dopant location and what has been devised experimentally, giving a good idea of the location of the heterometal within the framework. Notably, using only the first shell Mn–O scattering paths from the model yielded a substantially worse fit, with an R factor value of 0.023, compared to 0.013 when including the Mn–Zr paths
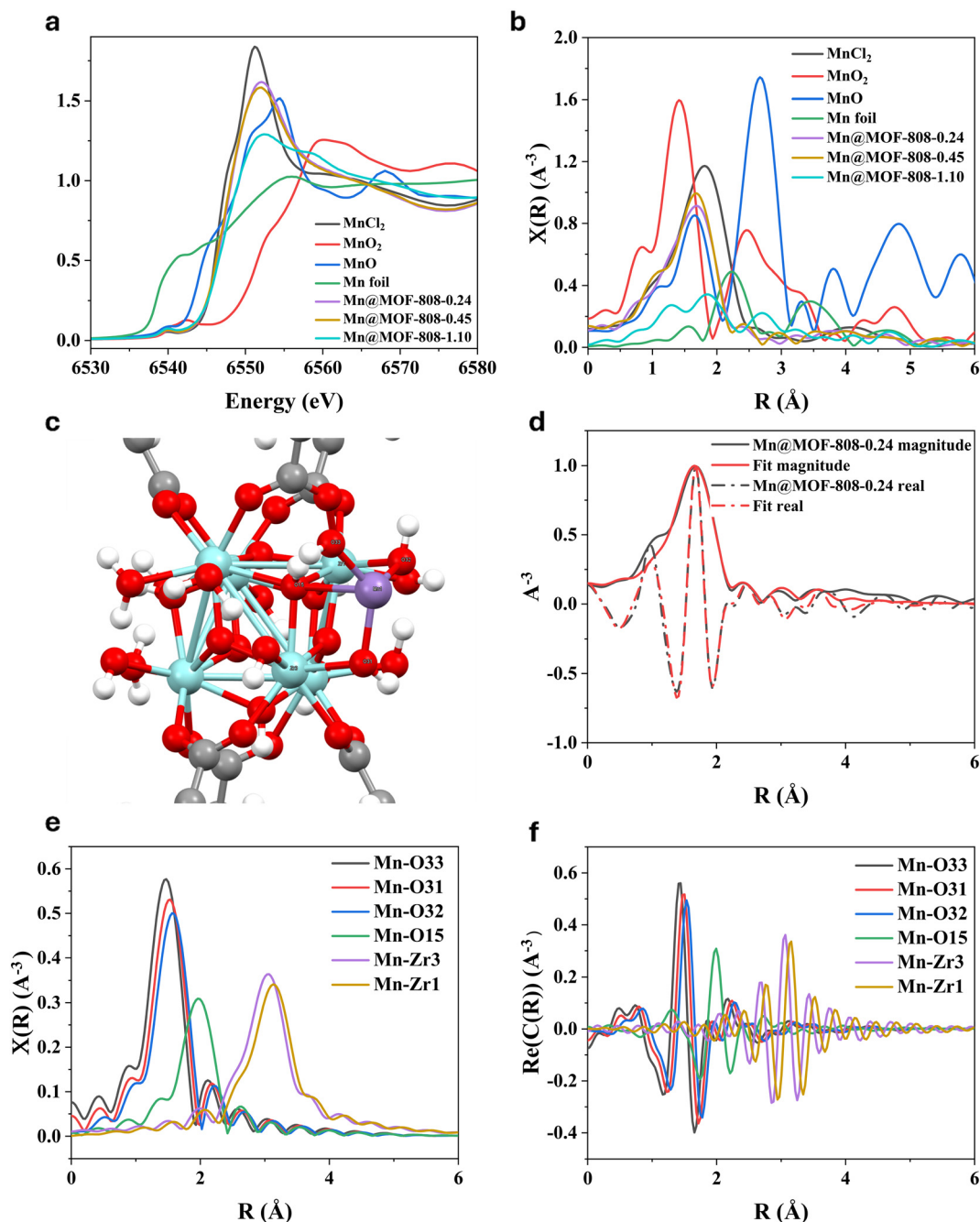
Fig. 2 Mn K-edge (a) XANES and (b) EXAFS spectra of Mn-doped MOF-808 frameworks and MnCl$_2$ MnO$_2$, MnO and Mn foil references. *R*-Space EXAFS spectra were obtained from the FT of the k^2-weighted *k*-space spectra over a *k*-range of 3 to 10 Å^{-1}. (c) Model of the Mn@MOF-808 metal cluster (atom colors: teal-Zr, purple-Mn, red-oxygen, gray-carbon, and white-hydrogen). (d) EXAFS fit of Mn@MOF-808-0.24, and the (e) scattering paths contributing to the fit. (f) Real *R*-space components of selected Mn@MOF-808-0.24 scattering paths.

(Fig. S6c and d, and Table S5). A more detailed description of this fitting procedure can be found in the SI.

Decomposition of DMNP and soman

The catalytic activity of MOF-808 and Mn@MOF-808 was initially assessed through the aqueous-phase (0.45 M *N*-ethylmorpholine buffered to pH 7) hydrolysis of the nerve agent simulant DMNP. The progression of the reaction was

monitored using electronic absorption spectroscopy by observing the absorption bands of DMNP (λ_{max} = 275 nm) and the hydrolysis products (Fig. 3a), 4-nitrophenolate (λ_{max} = 404 nm) and 4-nitrophenol (λ_{max} = 313 nm) over time (Fig. S8). The percent product conversion plots for each catalyst are shown in Fig. 3a. Mn doping did not significantly impact the DMNP degradation rate, as Mn@MOF-808 samples showed comparable conversion to pristine MOF-808 (Fig. 3c and Table S6). The half-lives for
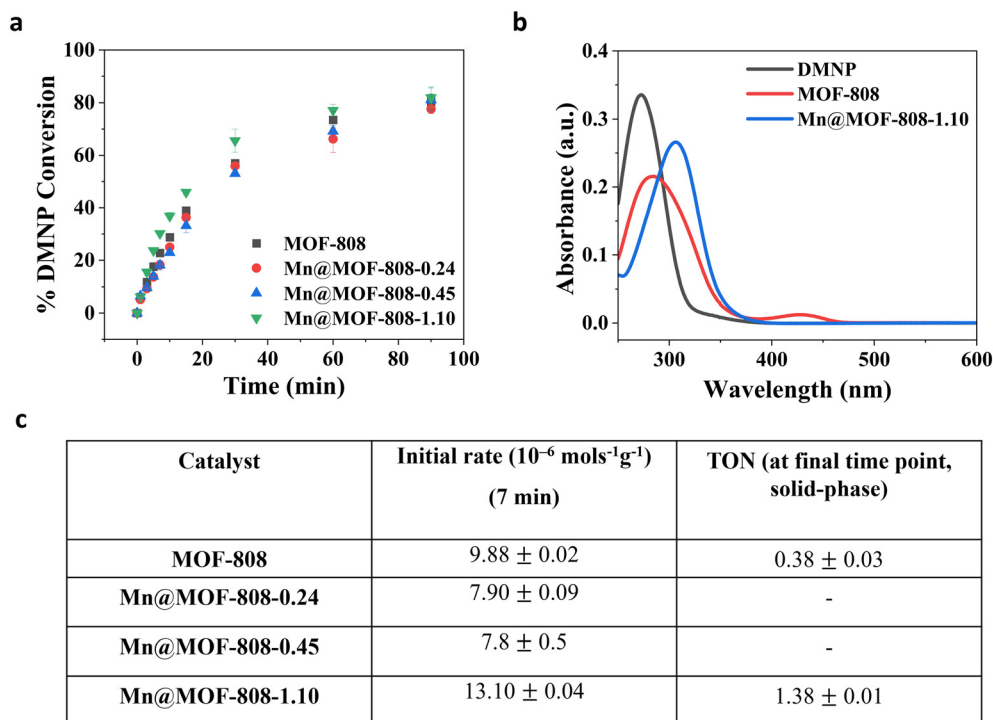
Catalyst	Initial rate (10^{-6} mol s^{-1} g^{-1}) (7 min)	TON (at final time point, solid-phase)
MOF-808	9.88 ± 0.02	0.38 ± 0.03
Mn@MOF-808-0.24	7.90 ± 0.09	-
Mn@MOF-808-0.45	7.8 ± 0.5	-
Mn@MOF-808-1.10	13.10 ± 0.04	1.38 ± 0.01

Fig. 3 (a) % DMNP conversion graphs of MOF-808 and Mn@MOF-808 catalysts in the aqueous phase, (b) DMNP hydrolysis profiles of MOF-808 and Mn@MOF-808-1.10 (solid-phase), (c) table displaying the initial reaction rate in aqueous-phase (at 7 min) and the TON in solid-phase (final time point) hydrolysis.

these reactions have been reported in Table S6. The stability and catalytic activity of the recycled samples were also evaluated and are detailed in SI section S4.4, Fig. S16–S20, and Table S11.

In a buffered aqueous-phase environment, bases aid in the removal of hydrolyzed products.[6] However, the pressing challenge remains in developing catalysts suitable for incorporation into personal protective equipment that can effectively degrade nerve agents in gas-phase environments where no base and limited water are available. To address this, we conducted real-time simulation hydrolysis studies in non-aqueous and unbuffered conditions. Our goal was to verify if single-atom modified catalysts could prevent catalyst poisoning and sustain a TON greater than 1, thus advancing this technology toward practical application. These studies were conducted by exposing neat DMNP to solid MOF catalysts and stirring the mixture for 2 weeks. The hydrolysis products were then extracted using acetonitrile, and Electronic Absorption Spectroscopy was employed to observe the absorption bands of DMNP (~272 nm) and the hydrolysis products (~309 and ~423 nm), as shown in Fig. 3b. In the presence of Mn@MOF-808-1.10, a higher conversion of DMNP was observed than in the native MOF (Fig. 3c and Table S7). Notably, Mn@MOF-808-1.10 facilitated a reaction with a TON exceeding 1, indicative of catalytic behavior. This represents the first reported case of a MOF-based catalyst achieving catalytic turnover (TON > 1) for nerve agent simulants under non-aqueous, unbuffered, and solid-phase conditions. No degradation was observed when DMNP was

stored under identical conditions without a catalyst (see SI section S4.5 and Fig. S23). The crystallinity and morphology were retained after the solid-phase hydrolysis reactions, as confirmed by the data in Fig. S9. As a complementary study, soman hydrolysis was also evaluated under non-aqueous conditions, showing degradation over a similar timescale, as detailed in SI section S4.6, Fig. S24 and Table S12. The result marks a critical milestone—demonstration of a TON > 1 under solid-phase conditions. In the following sections, we explore how the structural, spectroscopic, and mechanistic features of Mn@MOF-808-1.10 contribute to achieving this breakthrough performance.

Electronic structure calculations of the reaction mechanism for sarin hydrolysis

DFT calculations were employed to provide insights into the catalytic mechanism for sarin hydrolysis. The computational construction of the single-atom modified MOF-808 structure draws inspiration from prior work.[21,30] Briefly, each MOF-808 secondary building unit (SBU) of $Zr(IV)_6(\mu_3\text{-}O)_4(\mu_3\text{-}OH)_4$ stoichiometry is 6-connected to other SBUs *via* BTC linkers. The linkers are modeled in this work as benzoate capping ligands with C atoms held fixed in their crystallographic positions, as validated in the prior work.[30] A full coordination sphere for each Zr(IV) atom in the SBU was accomplished through the introduction of an aqua and a hydroxo ligand pair per Zr site. The functionalization of MOF-808 with Mn single atoms was achieved by inserting the single atom

between an aqua–hydroxo ligand pair, followed by proton removal to maintain charge neutrality (Fig. S10). The Mn atoms feature a terminal hydroxo ligand that acts as the base during hydrolysis and are anchored to the SBU via (μ_2-OH) or (μ_2-O) bridging ligands, depending on the oxidation state (II/IV) of the Mn single atom. As previously discussed, the experimental XAS and XPS results indicate that the Mn@MOF-808 samples are primarily composed of Mn(II)-inserted MOF-808, with a small contribution of Mn(IV)@MOF-808 likely at the MOF surface. Consequently, our focus will be on the Mn(II)@MOF-808 system, with data for Mn(IV)@MOF-808 provided for comparison. The mechanism discussed here for Mn@MOF-808 follows prior work on Zn(II) and Ti(IV) single atoms.[30]

The hydrolysis of sarin on Mn(II)@MOF-808 systems is described in Fig. 4a and begins upon sarin binding to the single atom via its phosphoryl oxygen (Cat-GB). Next, an ambient water molecule physisorbs in the vicinity of the single atom to furnish the reagent state (R). From R, the

water molecule protonates the Mn(II)–OHt base to generate a hydroxide nucleophile that concertedly adds to the phosphorus center of sarin in a single step (TS-add). A trigonal bipyramidal intermediate is formed following the nucleophilic addition (P5). The P5 intermediate decomposes through a low-barrier cleavage of the P–F bond (TS-eli), resulting in the elimination of HF and the formation of the isopropyl methyl phosphonic acid (IMPA) co-product (P). Subsequent desorption of HF from the P complex and of IMPA from the Cat-IMPA species regenerates the catalyst. Fig. S11 provides an analogous reaction mechanism for the hydrolysis of sarin on Mn(IV)@MOF-808; a comparative Gibbs energy diagram for both Mn@MOF-808 systems is provided in Fig. S12b. Fig. 4b shows that product desorption (170 kJ mol^{-1}) is more energetic than the addition transition state (70 kJ mol^{-1}).

As the experiments show, Mn@MOF-808-1.10 appears to be a more efficient catalyst than the native MOF-808. A plausible explanation for this result can be found comparing
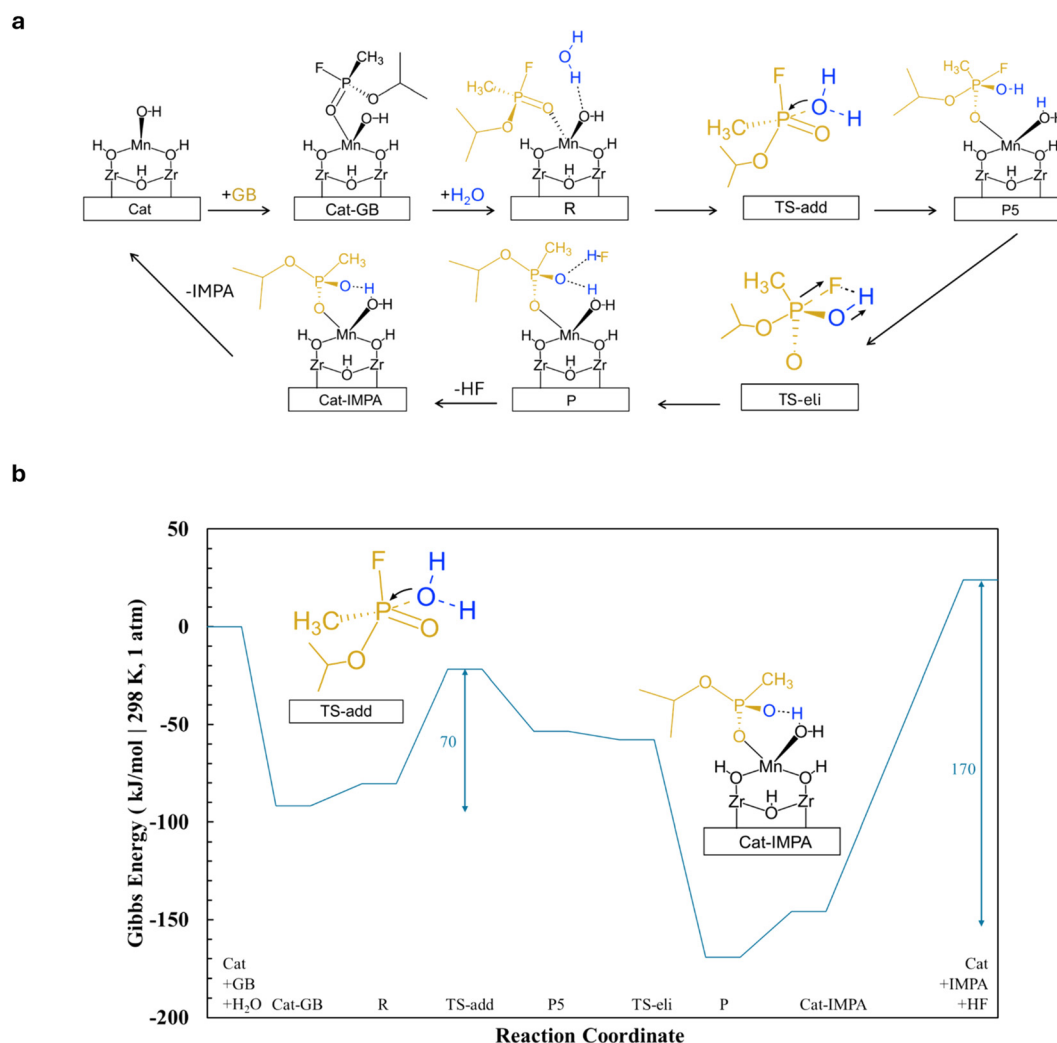

Fig. 4 (a) Reaction mechanism for the vacuum-phase hydrolysis of GB on Mn(II)@MOF-808. A ball-and-stick representation of this mechanism alongside the associated atomic coordinates is provided in Fig. S12a. (b) Gibbs energy profile for the vacuum-phase hydrolysis of GB on Mn(II)@MOF-808 following the mechanism in Fig. 4a and S12a.

the hydrolysis energy profiles of both materials. Fig. S12 shows that for Mn(II)@MOF-808, the IMPA product is bound in a monodentate fashion to the catalyst prior to rate-limiting desorption. Product desorption is also the most energetic step in the mechanism with the native MOF (Fig. S13). However, the adjacency of Zr sites on the native MOF allows for the possibility of bidentate binding of the phosphonate,[20] which leads to a more energetic desorption step compared to the Mn single-atom modified MOF-808 materials by 21 kJ mol^{-1}. This reduction in desorption energy explains the ability of Mn@MOF-808-1.10 to sustain catalytic turnover.

The DFT comparison indicates that the Mn(IV) site is intrinsically competent for sarin activation and, on a per-site basis, can exhibit a more favorable energetic profile for the hydrolysis sequence than Mn(II). However, bulk-sensitive XAS measurements establish that the majority of Mn in our materials resides in the +2 oxidation state (Fig. 2a), whereas XPS (a surface-sensitive probe) detects a small Mn(IV) contribution limited to the near-surface region. Taking these results together, we conclude that although Mn(IV) is intrinsically active according to our calculations, the overall catalytic behavior reported here is governed primarily by the more abundant Mn(II) sites. We have therefore focused our mechanistic discussion on Mn(II), while including Mn(IV) computations in the SI for reference and comparison.

Gas phase sarin degradation studies

To understand how Mn@MOF-808-1.10 achieves catalytic turnover in the gas phase, we probed the interaction of sarin with both unmodified and Mn-modified MOFs using *in situ* DRIFTS. The interaction and decomposition of sarin on MOF-808 and Mn@MOF-808-1.10 were studied, revealing key vibrational IR features and surface behaviors of these materials. The MOF samples were exposed to sarin vapor for 2 h, with spectra recorded every 60 s. The spectra of sarin and sarin-exposed MOFs (MOF-808 and Mn@MOF-808-1.10) are shown in Fig. 5a, with the vibrational IR features assigned in Fig. 5b. As MOF linkers are IR active, when sarin is exposed to the sample the vibrational intensity will change. Within a difference spectrum, these stretches are shown as decreasing with increased sarin exposure.[20] To focus on the most relevant data, Fig. 5a highlights a specific spectral region, while Fig. S14 shows the broader range.

Notably, vibrational stretches at 1275 cm^{-1} and 1231 cm^{-1} for MOF-808, and 1273 cm^{-1} and 1235 cm^{-1} for Mn@MOF-808-1.10 were observed, which correspond to P=O interacting with Zr atoms bonded to a linker or hydroxyls, respectively. These vibrational stretches are consistent with previous studies on sarin-exposed UiO-66.[31] On UiO-66, the band at 1235 cm^{-1} is predicted to be indicative of sarin H-bonding with a terminal hydroxyl; however, consumption of terminal hydroxyls was not observed in this study, as their
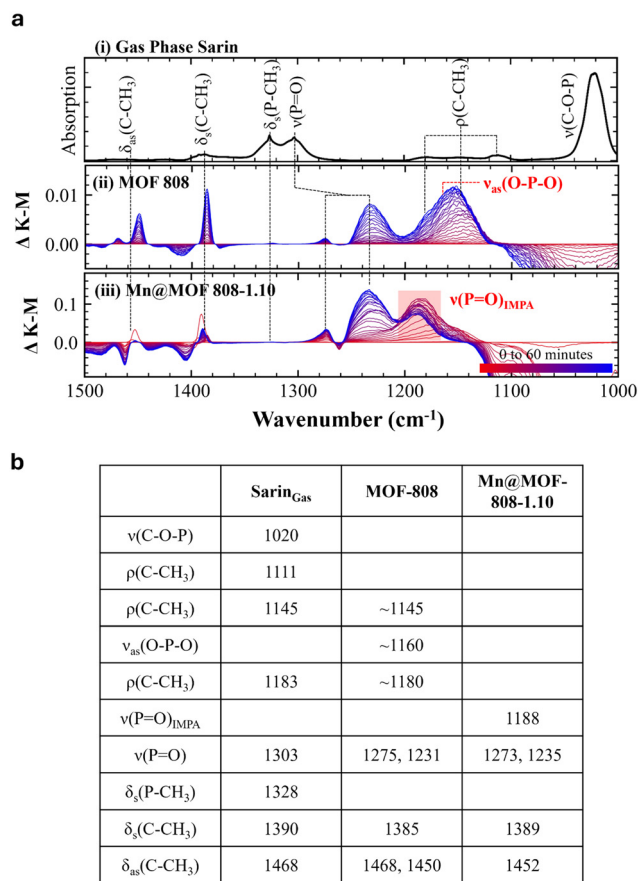

Fig. 5 (a) IR vapor phase spectra of (i) sarin and the *in situ* DRIFTS exposure of sarin onto (ii) MOF-808 and (iii) Mn@MOF-808-1.10. Sarin was exposed to the samples for 1 h, with the spectra moving from red to blue with increased exposure. Both MOF-808 and Mn@MOF-808-1.10 exhibit sarin decomposition; however, Mn@MOF-808-1.10 limits the formation of the typical O–P–O but produces the decomposition product, IMPA, interacting with the Zr node through the P=O. (b) Table showing peak assignments for gas-phase sarin and sarin-exposed MOF-808 and Mn@MOF-808-1.10. All values are reported in wavenumbers (cm^{-1}), and the peak assignments were determined from ref. 33, 34 and 36–39.

	Sarin$_{Gas}$	MOF-808	Mn@MOF-808-1.10
ν(C–O–P)	1020		
ρ(C–CH₃)	1111		
ρ(C–CH₃)	1145	~1145	
ν$_{as}$(O–P–O)		~1160	
ρ(C–CH₃)	1183	~1180	
ν(P=O)$_{IMPA}$			1188
ν(P=O)	1303	1275, 1231	1273, 1235
δ$_s$(P–CH₃)	1328		
δ$_s$(C–CH₃)	1390	1385	1389
δ$_{as}$(C–CH₃)	1468	1468, 1450	1452

typical adsorption peak at 3780 cm^{-1} (terminal OH) remained unaffected.[32] Instead, upon sarin adsorption, bands between 3696 cm^{-1} and 3640 cm^{-1} on MOF-808 and 3676 cm^{-1} and 3640 cm^{-1} on Mn@MOF-808-1.10, associated with higher-coordinated hydroxyls such as μ₃-OH, typically observed around 3674 cm^{-1}, are consumed. Consequently, the band at 1235 cm^{-1} is attributed to the P=O hydrogen bond with μ₃-OH. Intact sarin adsorbed onto an undercoordinated Zr site would result in a P=O stretch at approximately 1201 cm^{-1}.[31] As this stretch is not observed on either material, this suggests that if this site were to exist, it would promote rapid sarin decomposition.

A notable similarity between MOF-808 and Mn@MOF-808-1.10 is the absence of the δ$_s$(P–CH₃) vibrational mode, which could indicate either P–CH₃ cleavage or an interaction within

the MOF and P–CH$_3$ limiting a significant IR intensity, leaving the P–CH$_3$ cleavage pathway undetermined. The MOF-808 spectra exhibited symmetric and asymmetric δ(C–CH$_3$) vibrations at 1385 cm^{-1}, 1450 cm^{-1}, and 1468 cm^{-1}. Mn@MOF-808-1.10 displayed the corresponding IR features at 1389 cm^{-1} and 1452 cm^{-1} with reduced intensity, suggesting the cleavage of the P–OC$_3$H$_7$ mode.

The decomposition of sarin differs significantly between the two materials. Upon sarin decomposition, MOF-808 formed a bidentate O–P–O species ($\sim$1160 cm^{-1}),[33] a strongly bound structure that is difficult to remove.[21,34] In contrast, Mn@MOF-808-1.10 limits the creation of a bidentate species, but produces IMPA, adsorbed through P=O.[35,36] DRIFTS analysis confirms that Mn@MOF-808-1.10 avoids formation of strongly bound bidentate O–P–O intermediates observed in MOF-808, instead enabling IMPA desorption *via* the monodentate P=O interaction. A broad IR feature initially forms at 1154 cm^{-1}, which shifted to 1188 cm^{-1} and decreased in intensity over time and sarin exposure. Gas-phase IMPA v(P=O) absorbs at approximately 1226 cm^{-1}, but upon adsorption onto Mn@MOF-808-1.10, the band exhibits a red shift, making the most probable assignment for the peak at 1188 cm^{-1}, v(P=O).[36] This desorption behavior supports the observed catalytic activity, in contrast to MOF-808, which remains inhibited due to persistent bidentate product binding. Additionally, the IR feature at 1188 cm^{-1} hits a maximum and then decreases, and at the same time the P=O stretch for sarin interacting with a μ_3-OH appears. This decrease suggests that IMPA is desorbed from the surface with increased sarin exposure. Limiting the creation of bidentate species reduces the binding strength and facilitates desorption of the decomposition products. A similar trend was observed with DIFP exposure (Fig. S15). The findings confirm that Mn@MOF-808.1.10 limits the formation of strongly bound bidentate species, providing a structural rationale for its ability to surpass a TON = 1 in non-aqueous sarin and simulant degradation.

Conclusion

In this work, we demonstrate that incorporating Mn single atoms into MOF-808 significantly enhances its catalytic performance for nerve agent and simulant degradation. Structural analyses confirm that Mn modification retains the crystallinity, morphology, and porosity of the parent MOF. Among the materials studied, Mn@MOF-808-1.10 shows the most promising results, achieving a TON greater than 1 under solid-phase, unbuffered, and solvent-free conditions—representing the first example of catalytic turnover by a MOF-based system. Mechanistic studies suggest that Mn sites promote monodentate binding of hydrolysis products, which lowers the desorption energy of the product by approximately $\sim$21 kJ mol^{-1} relative to the unmodified framework. This shift prevents the catalyst poisoning typically caused by bidentate coordination. *In situ* DRIFTS analysis supports this mechanism, showing that Mn@MOF-808-1.10 suppresses the

formation of strongly bound O–P–O intermediates and allows efficient product removal during sarin and DIFP degradation. Taken together, these findings highlight the potential of node-level single-atom modification as a strategy to overcome catalyst deactivation in MOFs. This approach offers a path forward to designing solid-state, regenerable materials capable of operating under realistic conditions for chemical threat mitigation.

Author contributions

A. J. M., J. R. M., D. T., and C. J. K. conceived the project. A. S., M. K. J., N. K., and E. M. J. designed the experiments. C. F. performed DFT studies and contributed to writing the computational sections. C. L. L. and J. V. L. conducted and analyzed the XAS experiments and contributed to the corresponding text. M. Y. performed SEM analysis. M. C. B. carried out the IR analysis for MOF structural characterization and provided the write-up. M. B. L., A. B., H. W., and J. J. M. performed or assisted with nerve agent-related experiments and contributed to the elated text. A. S. drafted the main manuscript. All authors discussed the results and contributed to manuscript editing.

Conflicts of interest

A patent disclosure has been submitted on the technology discussed.

Data availability

The data supporting the findings of this study are available within the article and its supplementary information (SI). The input and output files for the DFT calculations are included as a separate ZIP file. Additional data are available from the corresponding author upon reasonable request.

Supplementary information is available. See DOI: https://doi.org/10.1039/d5cy00940e.

Acknowledgements

7556 | *Catal. Sci. Technol.*, 2025, **15**, 7549–7557

This journal is © The Royal Society of Chemistry 2025

References

1 View of comparative analysis of physicochemical characteristics of chemical warfare agents and their simulants, https://eskup.kpu.edu.rs/dar/article/view/446/217.

2 C. Hadad and O. Nosseir, *Chemical Agents & Countermeasures*, American Chemical Society, Washington, DC, USA, 2021.

3 M. Schwenk, *Toxicol. Lett.*, 2018, **293**, 253–263.

4 K. Ganesan, S. K. Raza and R. Vijayaraghavan, *J. Pharm. BioAllied Sci.*, 2010, **2**, 166–178.

5 R. T. Delfino, T. S. Ribeiro and J. D. Figueroa-Villar, *J. Braz. Chem. Soc.*, 2009, **20**, 407–428.

6 K. O. Kirlikovali, Z. Chen, T. Islamoglu, J. T. Hupp and O. K. Farha, *ACS Appl. Mater. Interfaces*, 2020, **12**, 14702–14720.

7 Y. Bai, Y. Dou, L.-H. Xie, W. Rutledge, J.-R. Li and H.-C. Zhou, *Chem. Soc. Rev.*, 2016, **45**, 2327–2367.

8 Y. Liu, A. J. Howarth, N. A. Vermeulen, S.-Y. Moon, J. T. Hupp and O. K. Farha, *Coord. Chem. Rev.*, 2017, **346**, 101–111.

9 M. J. Katz, J. E. Mondloch, R. K. Totten, J. K. Park, S. T. Nguyen, O. K. Farha and J. T. Hupp, *Angew. Chem., Int. Ed.*, 2014, **53**, 497–501.

10 B. Gibbons, E. C. Bartlett, M. Cai, X. Yang, E. M. Johnson and A. J. Morris, *Inorg. Chem.*, 2021, **60**, 16378–16387.

11 D. Bůžek, J. Demel and K. Lang, *Inorg. Chem.*, 2018, **57**, 14290–14297.

12 H. Wang, J. J. Mahle, T. M. Tovar, G. W. Peterson, M. G. Hall, J. B. DeCoste, J. H. Buchanan and C. J. Karwacki, *ACS Appl. Mater. Interfaces*, 2019, **11**, 21109–21116.

13 M. R. Momeni and C. J. Cramer, *J. Phys. Chem. C*, 2019, **123**, 15157–15165.

14 M. C. de Koning, M. van Grol and T. Breijaert, *Inorg. Chem.*, 2017, **56**, 11804–11809.

15 S.-Y. Moon, Y. Liu, J. T. Hupp and O. K. Farha, *Angew. Chem., Int. Ed.*, 2015, **54**, 6795–6799.

16 B. Picard, I. Chataigner, J. Maddaluno and J. Legros, *Org. Biomol. Chem.*, 2019, **17**, 6528–6537.

17 A. Zammataro, R. Santonocito, A. Pappalardo and G. Trusso Sfrazzetto, *Catalysts*, 2020, **10**, 881.

18 D. Troya, *J. Phys. Chem. C*, 2016, **120**, 29312–29323.

19 M. W. Terban, S. K. Ghose, A. M. Plonka, D. Troya, P. Juhás, R. E. Dinnebier, J. J. Mahle, W. O. Gordon and A. I. Frenkel, *Commun. Chem.*, 2021, **4**, 2.

20 G. Wang, C. Sharp, A. M. Plonka, Q. Wang, A. I. Frenkel, W. Guo, C. Hill, C. Smith, J. Kollar, D. Troya and J. R. Morris, *J. Phys. Chem. C*, 2017, **121**, 11261–11272.

21 M. L. Mendonca and R. Q. Snurr, *ACS Catal.*, 2020, **10**, 1310–1323.

22 E. M. Johnson, M. C. Boyanich, B. Gibbons, N. S. Sapienza, X. Yang, A. M. Karim, J. R. Morris, D. Troya and A. J. Morris, *Inorg. Chem.*, 2022, **61**, 8585–8591.

23 C. Cai, Q. Chen, H. Su, P. Huang, J. Mao and F.-Y. Wu, *Sci. China Mater.*, 2023, **66**, 2475–2482.

24 K. Ma, M. C. Wasson, X. Wang, X. Zhang, K. B. Idrees, Z. Chen, Y. Wu, S.-J. Lee, R. Cao, Y. Chen, L. Yang, F. A. Son, T. Islamoglu, G. W. Peterson, J. J. Mahle and O. K. Farha, *Chem Catal.*, 2021, **1**, 721–733.

25 H.-B. Luo, A. J. Castro, M. C. Wasson, W. Flores, O. K. Farha and Y. Liu, *ACS Catal.*, 2021, **11**, 1424–1429.

26 H.-B. Luo, F.-R. Lin, Z.-Y. Liu, Y.-R. Kong, K. B. Idrees, Y. Liu, Y. Zou, O. K. Farha and X.-M. Ren, *ACS Appl. Mater. Interfaces*, 2023, **15**, 2933–2939.

27 T. Wu, L. Guo, Q. Zhao, Y. Wu, D. Chen, C. Li and X. Jiao, *Appl. Surf. Sci.*, 2024, **662**, 160037.

28 H. Furukawa, F. Gándara, Y.-B. Zhang, J. Jiang, W. L. Queen, M. R. Hudson and O. M. Yaghi, *J. Am. Chem. Soc.*, 2014, **136**, 4369–4381.

29 A. M. Abdel-Mageed, B. Rungtaweevoranit, M. Parlinska-Wojtan, X. Pei, O. M. Yaghi and R. J. Behm, *J. Am. Chem. Soc.*, 2019, **141**, 5201–5210.

30 C. Fossum and D. Troya, *J. Phys. Chem. C*, 2024, **128**, 8983–8992.

31 J. A. Harvey, M. L. McEntee, S. J. Garibay, E. M. Durke, J. B. DeCoste, J. A. Greathouse and D. F. Sava Gallis, *J. Phys. Chem. Lett.*, 2019, **10**, 5142–5147.

32 D. Yang and B. C. Gates, *Adv. Mater.*, 2024, **36**, e2305611.

33 A. M. Plonka, T. G. Grissom, D. G. Musaev, A. Balboa, W. O. Gordon, D. L. Collins-Wildman, S. K. Ghose, Y. Tian, A. M. Ebrahim, M. B. Mitchell, C. L. Hill, J. R. Morris and A. I. Frenkel, *Chem. Mater.*, 2019, **31**, 9904–9914.

34 R. Tsyshevsky, M. McEntee, E. M. Durke, C. Karwacki and M. M. Kuklja, *ACS Appl. Mater. Interfaces*, 2021, **13**, 696–705.

35 R. J. Piffath, Infrared Spectroscopic Observations on the Fate of Organophosphorus Compounds Exposed to Atmospheric Moisture, *Part I. G-Agents and Related Compounds*, 2003, Defense Technical Information Center.

36 B. Yuan and H. Eilers, *Combust. Flame*, 2019, **199**, 69–84.

37 D. A. Panayotov and J. R. Morris, *J. Phys. Chem. C*, 2009, **113**, 15684–15691.

38 T. Hirakawa, K. Sato, A. Komano, S. Kishi, C. K. Nishimoto, N. Mera, M. Kugishima, T. Sano, H. Ichinose, N. Negishi, Y. Seto and K. Takeuchi, *J. Phys. Chem. C*, 2010, **114**, 2305–2314.

39 M. B. Leonard, E. Bruni, M. Hall, T. Li, E. E. Rodriguez and E. M. Durke, *J. Phys. Chem. Lett.*, 2022, **13**, 11663–11668.

This journal is © The Royal Society of Chemistry 2025

Catal. Sci. Technol., 2025, **15**, 7549–7557 | 7557